Journal of Clinical Neuroscience 144 (2026) 111803

Contents lists available at ScienceDirect

Journal of Clinical Neuroscience

journal homepage: www.journals.elsevier.com/journal-of-clinical-neuroscience

Original Research

Systematic machine learning approach for cerebral aneurysm feature selection and rupture status classification

Lior A. Kofman, Calvin G. Ludwig, Emal Lesha, Alexandra Lauric, Adel M. Malek *

Department of Neurosurgery, Tufts Medical Center and Tufts University School of Medicine, Boston, MA 02111, USA

ARTICLE INFO

Keywords:
Intracranial aneurysms
Machine learning
Caret
Aneurysm morphology
Aneurysm shape
Rupture status

ABSTRACT

Background: Current methods of intracranial aneurysm rupture risk assessment in the clinical setting depend on user measurements of morphological factors. Recently, machine learning (ML) has been proposed to assist in stratification of aneurysmal rupture risk. While numerous approaches have been taken, most rely on small sample sizes, restrict to specific anatomical locations, or manually balance ruptured and unruptured samples to enhance classification. By using 7 ML classifiers on a retrospective cohort of consecutive aneurysms distributed throughout the cranial vasculature, we present a computational tool that effectively classifies aneurysmal rupture status on a large, generalizable dataset.

Methods: Three-dimensional angiograms of patient cerebral aneurysms ($n = 678$; 229 ruptured and 449 unruptured aneurysms) enabled computation of 21 aneurysm features. Two datasets were used: morphological features only (MFO), and morphological plus 15 locational features (MLF). After normalization of numerical features and 7:3 training–testing splitting, for feature selection, a multivariate elastic network regression model was trained via 5-fold cross validation. Features were selected on the testing set. For classification, random 7:3 training–testing splitting was performed 100 times independently on each stratus. 8 classifiers (7 ML models and 1 generalized linear model; GLM) were used to assess rupture status. Area under the curve (AUC), sensitivity (SENS), and specificity (SPEC) were evaluated on testing sets. To elucidate the contribution of each feature to aneurysm rupture status assessment, feature importance was calculated for each optimal classifier.

Results: On the MFO dataset, multiple adaptive regression splines ($MARS_{MFO}$) exhibited the greatest performance ($AUC_{mean} = 0.797$, $SENS_{mean} = 0.777$, $SPEC_{mean} = 0.728$), with AUC also significant compared to GLM and three other ML classifiers. Aspect ratio (AR) and undulation index (UI) were the strongest factors. On the MLF dataset, neural networks ($NNET_{MLF}$) achieved the greatest performance ($AUC_{mean} = 0.825$, $SENS_{mean} = 0.803$, $SPEC_{mean} = 0.738$), followed by random forests (RF_{MLF}; $AUC_{mean} = 0.825$, $SENS_{mean} = 0.847$, $SPEC_{mean} = 0.710$). For $NNET_{MLF}$, AUC was found significant compared to GLM and three other ML classifiers. In neural networks, non-sphericity index (NSI), middle cerebral artery location, and AR were identified as the strongest contributors to rupture status.

Conclusion: We propose a systematic, user-independent approach to ML aneurysm rupture status classification. $MARS_{MFO}$ and $NNET_{MLF}$ exhibited the highest AUCs and outperform the traditional GLM, suggesting the utility of ML to assess intracranial rupture risk status. Morphological features such as NSI, UI, and AR were selected over maximal diameter, volume, and area. These factors may empower clinicians to accurately assess rupture risk, and they should be further studied.

1. Introduction

Incidental discovery of asymptomatic unruptured intracranial aneurysms (UIAs) has increased due to expanding access to sophisticated medical imaging technologies. Morphological evaluation of UIAs has been the focus of research, aiming to improve clinical prediction of rupture risk, to assist clinical decision making, and improve outcomes [1–3]. Aneurysmal subarachnoid hemorrhage carries a mortality rate of about 50 % and morbidity rate of 20–30 % [4]. Thus accurate prediction of rupture risk is critical to medical and surgical management of UIAs. Our study aims to better characterize UIA morphology and build methodologies to forecast rupture risk with improved accuracy.

* Corresponding author at: Department of Neurosurgery, Tufts Medical Center, 800 Washington Street, Boston, MA 02111, USA.
E-mail address: adel.malek@tuftsmedicine.org (A.M. Malek).

https://doi.org/10.1016/j.jocn.2025.111803
Received 26 September 2025; Accepted 4 December 2025
Available online 9 December 2025
0967-5868/© 2025 Elsevier Ltd. All rights are reserved, including those for text and data mining, AI training, and similar technologies.

The physical mechanism of aneurysmal rupture remains elusive. Several morphological descriptors have been evaluated in the prediction of aneurysm rupture status, including aneurysm size [1,5], height [6], aspect ratio [7], height to width ratio [8], size to parent vessel diameter ratio [9], inflow angle [10], and deviation from spherical or elliptical forms [11]. These features have been assessed on large samples of ruptured and unruptured aneurysms and are well established in the literature [12–14].

As in other medical fields, there is increased interest in applying machine learning (ML) to aneurysm rupture status prediction [15–27]. However, ML research remains in a novel stage, with best techniques for feature selection and data classification yet to be identified. The relationship between morphological features and rupture status, as well as interactions among these features, are not fully understood. Because these associations may follow complex, and potentially non-linear patterns, traditional linear statistical approaches may not fully capture the underlying structure of the data. Machine learning provides a promising framework for modeling such relationships by allowing algorithms to learn patterns, interactions, and decision boundaries directly from the data without requiring predefined assumptions about linearity.

This study proposes a systematic, user-independent approach to feature selection and classification using a robust dataset. To isolate the role of aneurysm morphology in rupture status discrimination, one variation of the analysis is performed using only morphological features. Due to the strong association between aneurysmal location with rupture status, and to further elucidate the interaction between morphological and locational features, we repeated the analysis using location information. Our aim here is to evaluate classification performance of established aneurysmal morphological features using a systematic application of 7 ML classifiers in the prediction of intracranial aneurysm rupture status, compared to a generalized, non-ML linear model.

2. Materials and methods

2.1. Patient selection

Patients undergoing cerebral angiography who were found to have intracranial aneurysms were included in this single-center, retrospective study. From these patients, consecutive high-resolution three-dimensional catheter-based cerebral angiographic data were reviewed for analysis. All pre-treatment angiographic studies, with sufficient image quality to permit accurate segmentation and isolation from surrounding vasculature, were used for morphological evaluation. For patients harboring ruptured aneurysms, angiographic data were obtained in emergent fashion and prior to vasospasm onset. Consequently, volumetric data were available for 678 aneurysms, of which 229 (33.8 %) were ruptured and 449 (66.2 %) were unruptured.

This research was approved by the Institutional Review Board ethics committee. Patient consent was waived because of the retrospective nature of the study not impacting patient clinical care.

2.2. Cerebral angiography and data processing

Three-dimensional catheter-based cerebral angiograms were obtained as previously described using a calibrated biplane system [28], with volume reconstruction using the available clinical software package, to yield a 3D volumetric dataset (Fig. 1A). Segmentation of aneurysm and parent vessels was performed using Amira 5.3 (FEI, Hillsboro, OR). Aneurysms were labeled as sidewall and bifurcation aneurysms as described by Baharoglu, *et al.* [13].

2.3. Feature extraction

Size and shape features were extracted as described in the literature

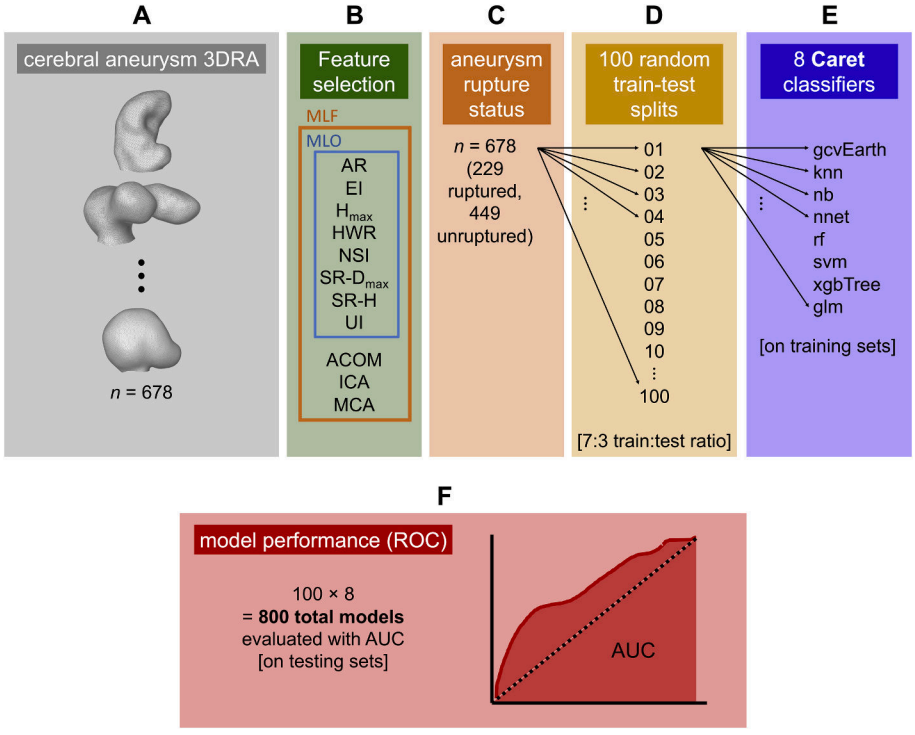


Fig. 1. Study process flow. (A) Data acquisition and image processing. Volumetric data was available for 678 aneurysms, of which 229 (33.4%) were ruptured. B) Feature selection. 11 and 7 features were selected from the MLF and MFO datasets, respectively. (C) Aneurysmal samples available for analysis. (D) Aneurysms were split into 100 train-testing groups. (E) Classification. 8 machine learning classifiers (extreme gradient boosting, multiple adaptive regression splines, k-nearest neighbors, naïve Bayes, neural networks, random forests, support vector machines, and generalized linear models) were applied to the dataset filtered for selected features. (F) Model performance. 800 classification models were applied to testing sets for area under the curve (AUC) of the receiver operating characteristic (ROC), used for model performance.

[28–30]. The aneurysms were isolated from the surrounding vessels and were represented as 3D mesh models using Amira 5.3 (Fig. 1A). The aneurysm neck plane was selected for each aneurysmal model and was represented as a triangular mesh model. The neck plane was selected to the best of our ability at the location where the aneurysmal sac protruded outward from the parent vessel [11,28,31]. A cross-sectional plane cut was selected proximally from the aneurysm neck at a distance of one vessel diameter on the inflow vessel. This parent vessel cross-sectional plane was similarly represented as a triangular mesh.

The resulting mesh models (aneurysm, neck plane, and inflow vessel plane) were used to automatically extract morphological features using an in-house Matlab tool (R2021; MathWorks, Natick, Massachusetts), previously described and validated [28].

21 morphological features were evaluated for each aneurysmal sample. Definitions are reproduced here for convenience: Maximal diameter (D_{max}) is the largest distance between any two points on the aneurysm mesh that could be fitted inside the aneurysmal dome. Maximal height is the largest distance between the center of the neck and the aneurysm surface that could be fitted inside the aneurysm dome. Center of the neck was defined as the centroid (geometric center) of the neck region [28]. Maximal width is the largest distance orthogonal to the maximal height. This is the maximum diameter along all cross sections orthogonal on the aneurysm maximal height. Volume is the volume of the mesh model. Area is the area of the mesh model. Neck size is twice the average distance from the neck centroid to neck border [32]. Parent vessel size defines twice the average distance from the parent vessel cross-section centroid to the parent vessel plane border [32]. Aspect ratio (AR) was computed as the height to neck ratio. Height-width ratio (HWR) is the height to width ratio. Bottleneck factor was defined as width to neck ratio. Size ratio based on height (SR-height) [33] is the ratio between maximal height and parent vessel size, whereas size ratio based on size (SR-D_{max}) was the ratio between maximal diameter and parent vessel size

3D morphological features, non-sphericity index (NSI), ellipticity index (EI) and undulation index (UI) [11], were automatically evaluated in Matlab. NSI quantifies the deviation of the aneurysmal shape from a sphere, an index of lesion instability previously associated with an increased risk of rupture. UI is the irregularity of the aneurysmal surface (e.g., lobulations, daughter sacs), with larger undulation indicating a more irregular shape. Finally, EI describes the physical resemblance of the aneurysmal model to an elliptical shape, with larger values indicating more elliptical features.

These features (Table 1) are established morphological features, extensively used in the literature for rupture status determination.

Table 1
Morphological, locational, and clinical features used to label rupture status of aneurysms. For numerical features, mean and standard deviation values are shown. For categorical features, raw count and proportion of the positive class are shown. Univariate statistical significance with rupture status, after multiple hypothesis adjustment via Bonferroni correction, was calculated. Asterisks (*) denote features with *p-adjusted* < *0.0001*.

Feature	Summary Statistic	P-adjusted Bonferroni
Ruptured aneurysms	229 (33.78 %)	
Aspect ratio, mean ± SD	1.39 ± 0.65	<0.0001*
Height-width ratio, mean ± SD	1.00 ± 0.27	<0.0001*
Non-sphericity index, mean ± SD	0.16 ± 0.11	<0.0001*
Size ratio (height), mean ± SD	2.16 ± 1.40	<0.0001*
Middle cerebral artery, n (%)	203 (29.94 %)	<0.0001*
Size ratio (Dmax), mean ± SD	2.78 ± 1.61	<0.0001*
Undulation index, mean ± SD	0.13 ± 0.14	<0.0001*
Maximal height, mean ± SD	5.35 ± 3.04	<0.0001*
Anterior communicating artery, n (%)	166 (24.48 %)	<0.0001*
Bottleneck, mean ± SD	1.38 ± 0.43	<0.0001*
Maximal diameter, mean ± SD	6.90 ± 3.46	<0.0001*
Area, mean ± SD	95.24 ± 113.19	0.0004
Orthogonal height, mean ± SD	4.21 ± 2.45	0.0023
Orthogonal width, mean ± SD	5.96 ± 3.12	0.0038
Volume, mean ± SD	120.33 ± 236.76	0.0119
Internal carotid artery, general, n (%)	56 (8.26 %)	0.0123
Maximum width, mean ± SD	5.41 ± 2.72	0.0344
Ellipticity index, mean ± SD	0.27 ± 0.07	0.2699
Sex, n (%)	519 (76.55 %)	0.2831
Posterior communicating artery, n (%)	140 (20.65 %)	0.4757
Posterior inferior cerebellar artery, n (%)	4 (0.59 %)	0.4988
Sidewall aneurysm, n (%)	207 (30.53 %)	1.0000
Age, mean ± SD	58.34 ± 13.71	1.0000
Maximal neck diameter, mean ± SD	4.38 ± 1.70	1.0000
Neck diameter, mean ± SD	3.44 ± 1.22	1.0000
Average neck diameter, mean ± SD	3.86 ± 1.39	1.0000
Neck area, mean ± SD	13.22 ± 10.48	1.0000
Orthogonal height-width ratio, mean ± SD	0.71 ± 0.21	1.0000
Anterior cerebral artery, A1 segment, n (%)	2 (0.29 %)	1.0000
Anterior cerebral artery, general, n (%)	5 (0.74 %)	1.0000
Anterior choroidal artery, n (%)	13 (1.92 %)	1.0000
Basilar artery, n (%)	27 (3.98 %)	1.0000
Internal carotid artery, bifurcation, n (%)	19 (2.8 %)	1.0000
Ophthalmic artery, n (%)	27 (3.98 %)	1.0000
Posterior cerebral artery, n (%)	4 (0.59 %)	1.0000
Pericallosal artery, n (%)	1 (0.15 %)	1.0000
Superior cerebellar artery, n (%)	7 (1.03 %)	1.0000
Vertebral artery, intracranial segment, n (%)	4 (0.59 %)	1.0000

2.4. Datasets

Two datasets with different subsets of features were employed in this analysis. First, a dataset comprised of only morphological features (MFO, $n = 21$) was used. With different aneurysmal locations strongly associated with rupture or unruptured risk [34,35], a second dataset included both morphological and location features (MLF, $n = 36$).

2.5. Statistical analysis

All statistical analysis, including dataset preparation, feature selection, machine learning classification, and model evaluation was performed in R Studio (version 2024.4.2.764) with R statistical programming software (version 4.4.0 "Puppy Cup"). **Caret** (version 6.0.94), **pROC** (version 1.18.5), and **dplyr** (1.1.4) were the R packages primarily used.

2.6. Feature selection

For the MFO and MLF datasets each, salient features were selected via elastic network (elastnet) regression (Fig. 1B). The data was split via a 7:3 training:testing ratio. The elastnet was trained and 5 cross-folds were used to find optimal model *lambda*, a parameter controlling the penalty applied to coefficients of features [36]. After running the optimal model on the test set, features with non-zero coefficients were selected.

2.7. Caret machine learning classification

To decrease the likelihood that classification results are specific to a particular random training–testing split, 100 pairs of training–testing sets in a 7:3 training:testing ratio were automatically generated among all aneurysms (Fig. 1D).

7 Caret ML classifiers and a generalized linear model (GLM) serving as a linear control were applied to each of the 100 feature groups from the training data, generating a total of 800 models (Fig. 1E). The response variable was a binary outcome: Ruptured or unruptured status. The detailed information of each Caret machine learning classifier is described in the Caret documentation (http://topepo.github.io/caret/)

The classifiers and Caret methods are as follows: multiple adaptive regression splines (gcvEarth); k-nearest neighbors (knn); naïve Bayes (nb); neural networks (nnet); random forests (rf); support vector machines (svmLinear2); extreme-gradient boosting (xgbTree), and generalized linear models (glm). Supplementary Table 1 provides additional methodological details for each model, including model type and basic algorithmic steps used for rupture-status classification.

2.8. Model and feature evaluation

For all 800 models, blind predictions of aneurysm rupture status were generated on the testing datasets using function **caret::predict.train**. These predictions were compared against the true rupture status of the corresponding aneurysms, enabling the creation of receiver operating characteristic (ROC) curves using the function **roc** in R package **pROC**. Area under the ROC curve (AUC) was used as the final metric of model performance (Fig. 1F). Model performance via mean AUC (AUC_{mean}) and AUC interquartile range (AUC_{IQR}) was evaluated. From the ROC curve, sensitivities and specificities were calculated using Youden's J statistic,[37] $J = sensitivity + specificity - 1$. For AUC, sensitivity, specificity, and accuracy, significance was measured between the classifier with the highest AUC_{mean} and all other classifiers, adjusted via Bonferroni correction.

The importance of features recruited for each of the eight classifiers was computed using the function **caret::varImp**. By default, variable importance for each feature is represented on a per-model arbitrary scale from 0 to 100. For the top classifier in the MLF dataset, feature interactions between morphological and locational features were computed via H-statistic [38]. The H-statistic defines the synergistic strength of two features, compared to their independent effects, on ruptured status. Partial dependence plots were generated via R, and curves were fit using Locally Estimated Scatterplot Smoothing [39].

3. Results

3.1. Patient demographics and intracranial location

Demographic information is summarized in Table 1. The combined dataset included 678 patient aneurysms, of which 229 (33.78 %) were ruptured. 76.55 % of patients were female. Sex was not found as a significant factor of rupture status (*adjusted $p = 1$ from unpaired, 2-sided Student's t-test*). The mean age of patients with ruptured aneurysms was *58.34*, representing a non-significant difference (*adjusted $p = 1$*). In addition, sidewall (*$n = 207$, 30.53 %*) or bifurcation status (*$n = 471$, 69.47 %*) was not a significant factor (*adjusted $p = 1$*). Three aneurysmal locations were found significantly associated with ruptured or unruptured status: middle cerebral artery (MCA, *adjusted $p < 0.0001$, $OR = 0.23$*), internal carotid artery (ICA, *adjusted $p = 0.012$, $OR = 0.26$*), and anterior communicating artery (ACOM, *adjusted $p < 0.0001$, $OR = 3.07$*).

3.2. Feature selection

For both the MFO and MLF datasets, significant features were filtered via multivariate elastic network regression. Of the 38 total features (2 demographic features, 15 location features, 21 morphological features), 7 and 11 features were selected, respectively (Fig. 2A-B). AUC of the testing MFO and MLF sets were 0.781 and 0.776 (Supplemental Table 2). Within the MLF dataset, all three significant locational features (MCA, ICA, and ACOM) were selected from the MLF.

3.3. Machine learning classifiers

For each classifier (8 total), a total of 100 models were created, one for each feature group (8 classifiers × 100 training sets = 800) (Supplemental Table 3). With the MFO dataset, the best performing classifier was $MARS_{MFO}$ (*$AUC_{mean} = 0.797$; $AUC_{IQR} = 0.775, 0.825$*), followed by RF_{MFO} (*$AUC_{mean} = 0.793$; $AUC_{IQR} = 0.763, 0.814$*) and $XGBTree_{MFO}$ (*$AUC_{mean} = 0.790$; $AUC_{IQR} = 0.760, 0.804$*). $MARS_{MFO}$ achieved significant AUC compared to GLM_{MFO}, SVM_{MFO}, NB_{MFO}, and KNN_{MFO} (*adjusted $p < 0.05$, two-sided t-test*) (Fig. 3). For the MLF dataset, the best performing classifier was $NNET_{MLF}$ (*$AUC_{mean} = 0.825$; $AUC_{IQR} = 0.801, 0.846$*), followed by RF_{MLF} (*$AUC_{mean} = 0.825$; $AUC_{IQR} = 0.798, 0.844$*) and $MARS_{MLF}$ (*$AUC_{mean} = 0.824$; $AUC_{IQR} = 0.806, 0.835$*). $NNET_{MLF}$, with the greatest AUC_{mean}, performed significantly better than GLM_{MLF}, KNN_{MLF}, NB_{MLF}, and SVM_{MLF} (*adjusted $p < 0.05$, two-sided t-test*) (Fig. 4).

In addition to producing the highest AUC values compared to other classifiers, $MARS_{MFO}$ and $NNET_{MLF}$ exhibited balanced sensitivities and specificities. For $MARS_{MFO}$, *$SENS_{mean} = 0.770$ ($SENS_{IQR} = 0.762, 0.788$)* and *$SPEC = 0.734$ ($AUC_{IQR} = 0.782, 0.809$)*. For $NNET_{MLF}$, *$SENS_{mean} = 0.810$ ($SENS_{IQR} = 0.742, 0.861$)* and *$SPEC = 0.730$ ($AUC_{IQR} = 0.698,$*

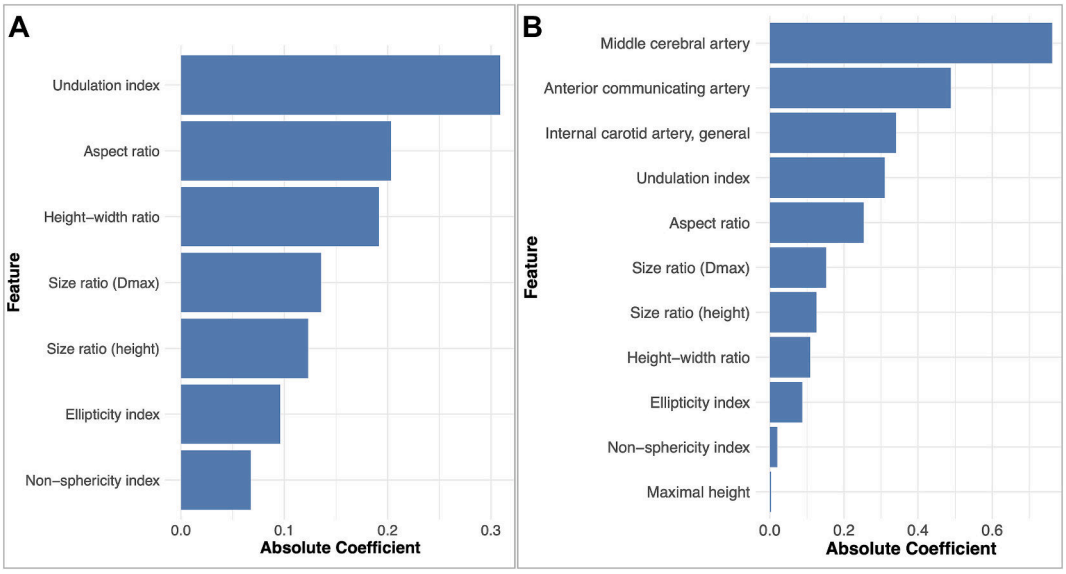


Fig. 2. Features selected following multivariate elastic network regression. All features shown were selected due to elastic network regression *coefficient ≠ 0*. (A) Selected features from MLF. (B) Selected features from MFO.

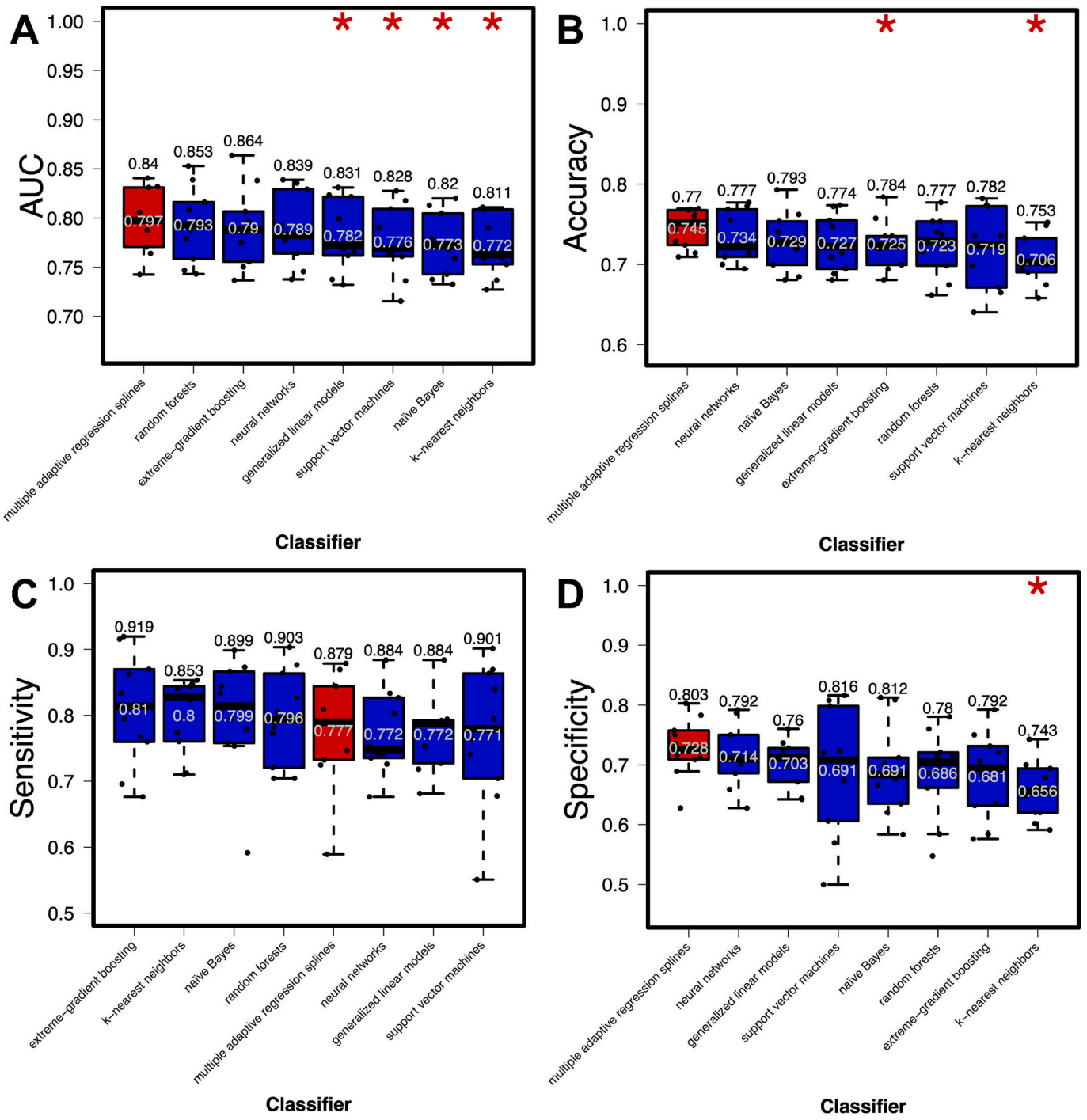


Fig. 3. MFO Classifier Results. Box plot of 100-model performance of each classifier. Shown are 25th and 75th percentiles, mean values, and range values of the best performing models. Asterisks (*) denote classifiers found with a significantly different performance metric compared to the highest-AUC classifier. Classifiers ordered by mean metric value. (A) AUC of ROC; (B) Sensitivity; (C) Specificity; (D) Accuracy.

0.748).

Feature importance was computed for these two high-performance models. For $MARS_{MFO}$, the most important features were AR and UI (Fig. 5A). Both features had a mean relative importance of $>$ 80 %, indicating they largely drove aneurysmal ruptures in this dataset-classifier combination. No other feature had a maximum importance of $>$ 40 % or an importance that was higher than these two features in any of the splits analyzed by $MARS_{MFO}$.

For $NNET_{MLF}$, the most important features were MCA location, NSI, AR, and UI (Fig. 5B). To elucidate possible synergistic interactions, Friedman's H-statistic was calculated for all possible pairs of morphological and locational features (Table 2). With the lowest $H = 0.776 \pm 0.048$, all morphological-locational pairs exhibited moderate to strong interactions. The strongest interactions were NSI-ICA, NSI-ACOM, and NSI-MCA; partial dependence plots of these feature pairs are shown in Fig. 5C. Cutoffs for rupture risk widely vary depending on location, as rupture risk remains low for any NSI value in ICA aneurysms. For ACOM aneurysms, rupture risk exceeds a predicted probability of 0.5 at NSI = –0.376, while for MCA aneurysms this threshold occurs at NSI = 0.725. Rupture risk exhibits a positive relationship with NSI in MCA

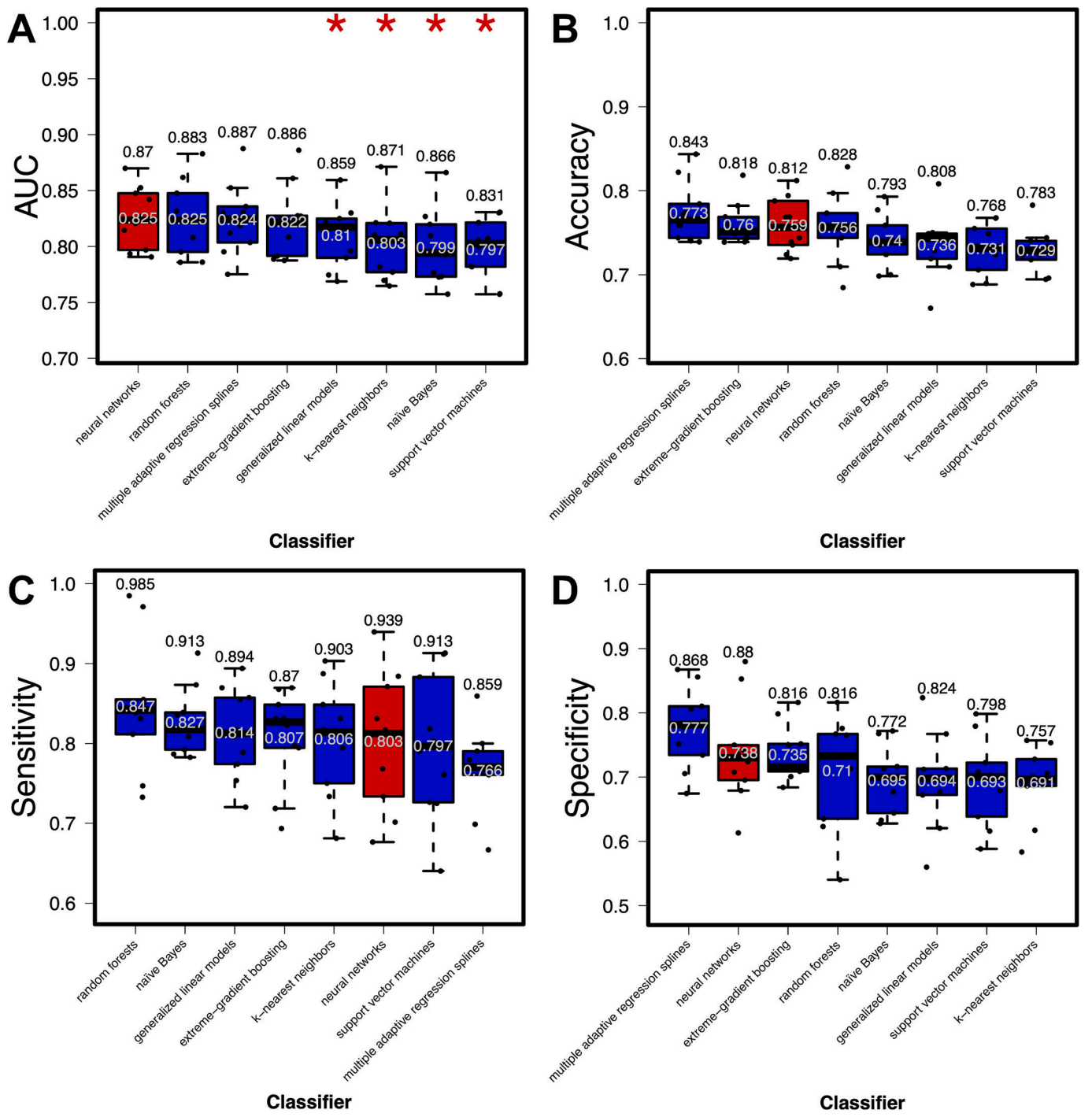


Fig. 4. MLF Classifier Results. Box plot of 100-model performance of each classifier. Shown are 25th and 75th percentiles, mean values, and range values of the best performing models. Asterisks (*) denote classifiers found with a significantly different performance metric compared to the highest-AUC classifier. Classifiers ordered by mean metric value. (A) AUC of ROC; (B) Sensitivity; (C) Specificity; (D) Accuracy.

aneurysms, markedly different from the negative association between rupture risk and MCA location alone.

4. Discussion

The factors contributing to rupture status of intracranial aneurysms are not fully elucidated. Per the American Heart Association and American Stroke Association, rupture risk stratification is currently still based predominantly on aneurysm size [40]. However, size alone does not comprehensively capture rupture risk, with anatomical location and morphology posited as salient features [41]. In this paper, we sought to model the classification of rupture status using these features by applying a broad range of analytical approaches. To capture the potential complex relationship between morphological and location characteristics and aneurysm rupture status, we employed multiple machine learning algorithms. By evaluating a wide variety of models that differ in how they incorporate and weight features, we present a systematic assessment of rupture status classification using ML.

To effectively compare the performance of ML classifiers with traditional linear models, we focused on curating a robust dataset. With

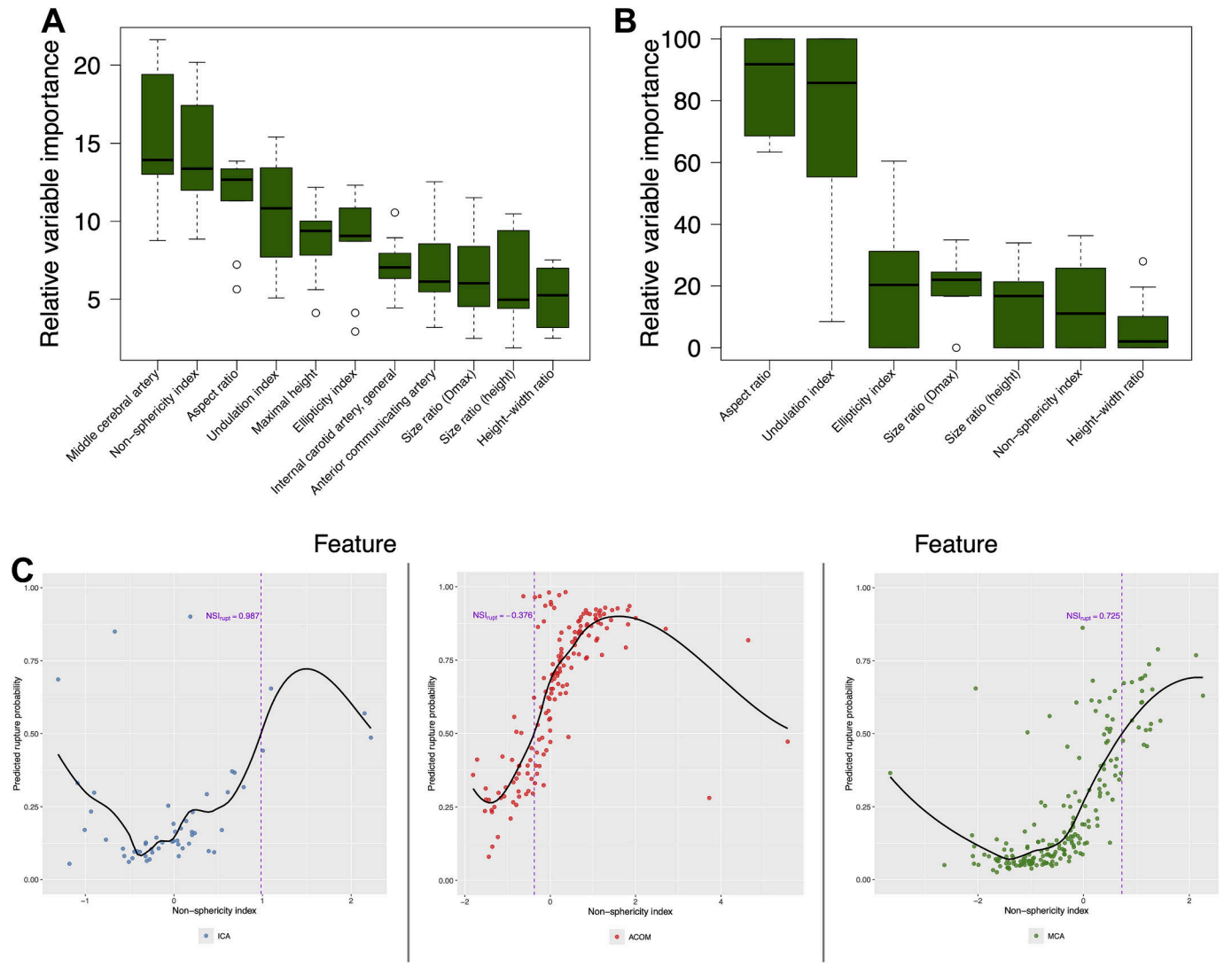


Fig. 5. Box plot of relative variable importance for features from top performing classifiers. Shown are 25th and 75th percentiles, mean values, and range values of features. Features were ordered by mean variable importance. (A) Multiple adaptive regression splines run on MFO ($MARS_{MFO}$); (B) neural networks run on MLF ($NNET_{MLF}$). Partial-dependence plots of predicted rupture probabilities from strongest morphology-location pairwise feature interactions. Curve shown was fit via Locally Estimated Scatterplot Smoothing (LOESS). Dotted vertical line indicates NSI_{rupt}, the lowest NSI at which predicted probability of rupture > 0.5 on the fitted curve. (C) NSI-ICA; NSI-ACOM; NSI-MCA.

678 total consecutive aneurysms used from numerous intracranial locations, our data offers a powerful, generalizable sample set for ML classifiers to train and test on. Previous studies commonly suffer from at least one of the following limitations: small sample size [16,19,23,25], oversampled rupture classes [16,18,23] and restriction to certain intracranial locations [19,20,24]. Detailed information regarding previous relevant literature is available as Supplementary Table 4.

Before classifying aneurysm rupture status, we sought to determine which features were the most salient. We evaluated two versions of the feature set: one restricted to morphological features only (MFO) and another incorporating both morphological and locational features (MLF). Feature selection serves to systematically mitigate human errors in feature curation. Without filtering feature sets may suffer from (1) subjective decision regarding feature importance, (2) presence of confounding variables, and (3) redundancy among features. Numerous previous efforts did not apply feature selection before classifying rupture status [20,21,23,25,27]. Using multivariate regression, morphological features such as NSI, UI, and AR were consistently selected, whereas traditional size-based features, such as volume and area, were not selected in either the MLF or MFO sets, indicating their comparatively lower utility in estimating rupture risk.

In order to identify optimal ML models to classify rupture risk, we selected a broad range of ML approaches that incorporate different strategies for classification, including decision trees, piecewise linear functions, dimension analysis, probability analysis, and neural networks. Previous studies have typically evaluated only a limited set of classifiers [17,20,23,24] and did not compare performances against traditional linear models. Our comprehensive analysis showed that, on the MFO dataset, multiple adaptive regression splines achieved the greatest AUC_{mean} ($AUC_{mean} = 0.797$, $SENS_{mean} = 0.777$, $SPEC_{mean} = 0.728$), followed by random forests. On the MLF dataset, neural networks achieved the greatest AUC_{mean} ($AUC_{mean} = 0.825$, $SENS_{mean} = 0.803$, $SPEC_{mean} = 0.738$), followed by random forests.

Following classification we assessed the most influential features and the interactions among these features In the $MARS_{MFO}$ model, AR and UI emerged as the most important features. For $NNET_{MLF}$, MCA location, NSI, AR, and UI were identified as the strongest discriminating factors. The most prominent morphological-location interactions were NSI-ICA (internal carotid artery), NSI-ACOM (anterior communicating artery), and NSI-MCA (middle cerebral artery). With H-statistic values greater

Table 2
Pairwise feature interactions for all morphological-locational feature pairs from neural network models run on all testing MLF datasets. H-statistic shown represents the mean and standard deviation H-statistic from all iterations.

Feature x	Feature y	H-statistic
Non-sphericity index	Internal carotid artery, general	1.073 ± 0.039
Non-sphericity index	Anterior communicating artery	1.065 ± 0.048
Non-sphericity index	Middle cerebral artery	1.044 ± 0.051
Maximal height	Internal carotid artery, general	1.042 ± 0.021
Maximal height	Anterior communicating artery	1.038 ± 0.028
Maximal height	Middle cerebral artery	1.015 ± 0.019
Size ratio (height)	Internal carotid artery, general	1.005 ± 0.029
Size ratio (height)	Anterior communicating artery	0.992 ± 0.04
Size ratio (height)	Middle cerebral artery	0.971 ± 0.051
Ellipticity index	Internal carotid artery, general	0.969 ± 0.013
Ellipticity index	Anterior communicating artery	0.955 ± 0.02
Height-width ratio	Internal carotid artery, general	0.945 ± 0.044
Ellipticity index	Middle cerebral artery	0.932 ± 0.024
Height-width ratio	Anterior communicating artery	0.93 ± 0.036
Height-width ratio	Middle cerebral artery	0.911 ± 0.052
Size ratio (Dmax)	Internal carotid artery, general	0.895 ± 0.029
Size ratio (Dmax)	Anterior communicating artery	0.872 ± 0.026
Undulation index	Internal carotid artery, general	0.842 ± 0.028
Aspect ratio	Internal carotid artery, general	0.832 ± 0.055
Size ratio (Dmax)	Middle cerebral artery	0.822 ± 0.049
Undulation index	Anterior communicating artery	0.805 ± 0.03
Undulation index	Middle cerebral artery	0.803 ± 0.029
Aspect ratio	Anterior communicating artery	0.799 ± 0.062
Aspect ratio	Middle cerebral artery	0.776 ± 0.048

than 1, these feature pairs demonstrated highly synergistic effects, indicating that their combined influence on rupture status is greater than the sum of their individual contributions [38]. Different thresholds of NSI confer higher rupture risk across the three significant aneurysmal locations (*NSI-ICA = 0.987, NSI-ACOM = -0.376, NSI-MCA = 0.725*), highlighting the importance of location when using morphology to estimate rupture risk. In both the MLF and MFO datasets, shape morphological features outperform size-based morphological features, such as D_{max} and height, featured used in the clinical setting. This study shows that features such as NSI, UI, and AR, may provide clinicians with much more powerful assessments of rupture risk. They should be further studied with respect to aneurysmal location to understand their synergistic relationship with rupture risk, and larger studies will be needed to validate these interactions and their potential clinical relevance.

4.1. Study limitations

The current study is retrospective and used for classification of previously determined rupture status, rather than prediction. As such, it is not intended as a predictive tool for rupture risk. Retrospective analysis depends on the hypothesis that aneurysms do not change size and shape after rupture. Like other retrospective investigations, this design limits our ability to infer causality or determine whether observed differences represent predictive markers or reflect post-rupture alterations. Conclusive data on this subject remain to be found, and large prospective studies will be needed to validate the clinical merit of our study.

5. Conclusion

We propose and evaluate a systematic, user-independent methodology of machine learning classification of intracranial aneurysm rupture status. This study introduces several key contributions compared with prior literature: the use of a large, consecutive, multi-location cohort reflective of population-level rupture status proportions; a user-independent multivariate feature-selection approach; a comprehensive and repeated comparison of eight machine-learning models; and the identification of synergistic interactions between morphological and locational features. Our tool employs feature selection, machine learning classification, and model evaluation against a generalized linear model control. Models built with deep learning ($NNET_{MLF}$) and multiple adaptive regression splines ($MARS_{MFO}$) feature greater mean AUC ($AUC_{mean} = 0.825$ and $AUC_{mean} = 0.797$, respectively) than linear models and several other machine learning algorithms. 3D morphological features such as non-sphericity index, undulation index, and aspect ratio were the most important features in the high-performance classifiers. By quantifying interactions between morphology and location, we determined clinically relevant thresholds for rupture status based on morphology and location. Further investigation is warranted to clarify how morphology and intracranial location influence rupture risk, and to validate our findings in order to determine how they can be integrated into clinical workflows.

6. IRB approval

This research was approved by Tufts Health Sciences Campus Institutional Review Board (IRB# 9035). Patient consent was waived because of the retrospective nature of the study not impacting patient clinical care.

7. Sources of support

None.

Ethical statement

This research was approved by Tufts Health Sciences Campus Institutional Review Board (IRB# 9035). All procedures were performed in compliance with relevant laws and institutional guidelines and have been approved by the appropriate institutional committee. Patient consent was waived because of the retrospective nature of the study not impacting patient clinical care.

CRediT authorship contribution statement

Lior A. Kofman: Writing – review & editing, Methodology, Investigation, Data curation. **Calvin G. Ludwig:** Writing – original draft, Methodology, Investigation, Data curation. **Emal Lesha:** Investigation, Data curation. **Alexandra Lauric:** Writing – review & editing, Supervision, Data curation. **Adel M. Malek:** Writing – review & editing, Supervision, Methodology, Formal analysis, Data curation, Conceptualization.

Declaration of competing interest

The authors declare that they have no known competing financial interests or personal relationships that could have appeared to influence the work reported in this paper.

Appendix A. Supplementary data

Supplementary data to this article can be found online at https://doi.org/10.1016/j.jocn.2025.111803.

References

[1] Wiebers DO, Whisnant JP, O'Fallon WM. The natural history of unruptured intracranial aneurysms. N Engl J Med 1981;304:696–8.
[2] Wiebers DO. Patients with small, asymptomatic, unruptured intracranial aneurysms and no history of subarachnoid hemorrhage should generally be treated conservatively: for. Stroke 2005;36:408–9.
[3] Juvela S. Treatment options of unruptured intracranial aneurysms. Stroke 2004;35:372–4.
[4] van Gijn J, Kerr RS, Rinkel GJE. Subarachnoid haemorrhage. Lancet 2007;369:306–18.
[5] Wiebers DO, Whisnant JP, Huston 3rd J, Meissner I, Brown Jr RD, Piepgras DG, et al. Unruptured intracranial aneurysms: natural history, clinical outcome, and risks of surgical and endovascular treatment. Lancet 2003;362:103–10.

[6] Mocco J, Brown Jr RD, Torner JC, Capuano AW, Fargen KM, Raghavan ML, et al. Aneurysm morphology and prediction of rupture: an international study of unruptured intracranial aneurysms analysis. Neurosurgery 2018;82:491–6.
[7] Ujiie H, Tachibana H, Hiramatsu O, Hazel AL, Matsumoto T, Ogasawara Y, et al. Effects of size and shape (aspect ratio) on the hemodynamics of saccular aneurysms: a possible index for surgical treatment of intracranial aneurysms. Neurosurgery 1999;45:119–30.
[8] Hoh BL, Sistrom CL, Firment CS, Fautheree G, Velat G, Whiting J, et al. Bottleneck factor and height-width ratio: association with ruptured aneurysms in patients with multiple cerebral aneurysms. Neurosurgery 2007;61:716–23.
[9] Rahman M, Smietana J, Hauck E, Hoh B, Hopkins N, Siddiqui A, et al. Size ratio correlates with intracranial aneurysm rupture status: a prospective study. Stroke 2010;41:916–20.
[10] Baharoglu M, Schirmer C, Hoit D, Gao B, Malek A. Aneurysm inflow-angle as a discriminant for rupture in sidewall cerebral aneurysms: morphometric and computational fluid dynamic analysis. Stroke 2010;41:1423–30.
[11] Raghavan ML, Ma B, Harbaugh RE. Quantified aneurysm shape and rupture risk. J Neurosurg 2005;102:355–62.
[12] Detmer FJ, Chung BJ, Jimenez C, Hamzei-Sichani F, Kallmes D, Putman C, et al. Associations of hemodynamics, morphology, and patient characteristics with aneurysm rupture stratified by aneurysm location. Neuroradiology 2019;61:275–84.
[13] Baharoglu MI, Lauric A, Gao B-L, Malek AM. Identification of a dichotomy in morphological predictors of rupture status between sidewall- and bifurcation-type intracranial aneurysms. J Neurosurg 2012;116:871–81.
[14] Liu J, Chen Y, Zhu D, Li Q, Chen Z, Zhou J, et al. A nomogram to predict rupture risk of middle cerebral artery aneurysm. Neurol Sci 2021.
[15] Liu J, Chen Y, Lan L, Lin B, Chen W, Wang M, et al. Prediction of rupture risk in anterior communicating artery aneurysms with a feed-forward artificial neural network. Eur Radiol 2018;28:3268–75.
[16] Niemann U, Berg P, Niemann A, Beuing O, Preim B, Spiliopoulou M, et al. Rupture status classification of intracranial aneurysms using morphological parameters. In: 2018 IEEE 31st International Symposium on Computer-Based Medical Systems (CBMS); 2018. p. 48–53.
[17] Walther G, Martin C, Haase A, Nestler U, Schob S. Machine learning for rupture risk prediction of intracranial aneurysms: challenging the PHASES score in geographically constrained areas. Symmetry 2022;14:943.
[18] Xiong W, Chen T, Li J, Xiang L, Zhang C, Xiang L, et al. Interpretable machine learning model to predict rupture of small intracranial aneurysms and facilitate clinical decision. Neurol Sci 2022;43:6371–9.
[19] Lin M, Xia N, Lin R, Xu L, Chen Y, Zhou J, et al. Machine learning prediction model for the rupture status of middle cerebral artery aneurysm in patients with hypertension: a Chinese multicenter study. Quant Imaging Med Surg 2023;13:4867–78.
[20] Kim HC, Rhim JK, Ahn JH, Park JJ, Moon JU, Hong EP, et al. Machine learning application for rupture risk assessment in small-sized intracranial aneurysm. J Clin Med 2019;8:683.
[21] Silva MA, Patel J, Kavouridis V, Gallerani T, Beers A, Chang K, et al. Machine learning models can detect aneurysm rupture and identify clinical features associated with rupture. World Neurosurg 2019;131:e46–51.
[22] Detmer FJ, Lückehe D, Mut F, Slawski M, Hirsch S, Bijlenga P, et al. Comparison of statistical learning approaches for cerebral aneurysm rupture assessment. Int J Comput Assist Radiol Surg 2020;15:141–50.
[23] Tanioka S, Ishida F, Yamamoto A, Shimizu S, Sakaida H, Toyoda M, et al. Machine learning classification of cerebral aneurysm rupture status with morphologic variables and hemodynamic parameters. Radiol Artif Intell 2020;2:e190077.
[24] Zhu W, Li W, Tian Z, Zhang Y, Wang K, Zhang Y, et al. Stability assessment of intracranial aneurysms using machine learning based on clinical and morphological features. Transl Stroke Res 2020;11:1287–95.
[25] Chen R, Mo X, Chen Z, Feng P, Li H. An integrated model combining machine learning and deep learning algorithms for classification of rupture status of IAs. Front Neurol 2022;13:868395.
[26] Shu Z, Chen S, Wang W, Qiu Y, Yu Y, Lyu N, et al. Machine learning algorithms for rupture risk assessment of intracranial aneurysms: a diagnostic meta-analysis. World Neurosurg 2022;165:e137–47.
[27] Shi Z, Chen GZ, Mao L, Li XL, Zhou CS, Xia S, et al. Machine learning–based prediction of small intracranial aneurysm rupture status using CTA-derived hemodynamics: a multicenter study. Am J Neuroradiol 2021;42:648–54.
[28] Lauric A, Baharoglu MI, Malek AM. Ruptured status discrimination performance of aspect ratio, height/width, and bottleneck factor is highly dependent on aneurysm sizing methodology. Neurosurgery 2012;71:38–46.
[29] Lauric A, Ludwig CG, Malek AM. Enhanced radiomics for prediction of rupture status in cerebral aneurysms. World Neurosurg 2022;159:e8–22.
[30] Ludwig CG, Lauric A, Malek JA, Mulligan R, Malek AM. Performance of radiomics derived morphological features for prediction of aneurysm rupture status. J Neurointervent Surg 2020.
[31] Xiang J, Natarajan SK, Tremmel M, Ma D, Mocco J, Hopkins LN, et al. Hemodynamic-morphologic discriminants for intracranial aneurysm rupture. Stroke 2011;42:144–52.
[32] Dhar S, Tremmel M, Mocco J, Kim M, Yamamoto J, Siddiqui AH, et al. Morphology parameters for intracranial aneurysm rupture risk assessment. Neurosurgery. 2008;63:185-96; discussion 96-7.
[33] Wang G-X, Liu L-L, Wen L, Cao Y-X, Pei Y-C, Zhang D. Morphological characteristics associated with rupture risk of multiple intracranial aneurysms. Asian Pac J Trop Med 2017;10:1011–4.
[34] Juvela S, Porras M, Heiskanen O. Natural history of unruptured intracranial aneurysms: a long-term follow-up study. J Neurosurg 1993;79:174–82.
[35] Juvela S, Poussa K, Lehto H, Porras M. Natural history of unruptured intracranial aneurysms: a long-term follow-up study. Stroke 2013;44:2414–21.
[36] Zou H, Hastie T. Regularization and variable selection via the elastic net. J R Stat Soc Ser B Stat Methodol 2005;67:301–20.
[37] Youden WJ. Index for rating diagnostic tests. Cancer 1950;3:32–5.
[38] Friedman JH, Popescu BE. Predictive learning via rule ensembles. Ann Appl Stat 2008;2:916–54.
[39] Cleveland WS, Devlin SJ. Locally weighted regression: an approach to regression analysis by local fitting. J Am Stat Assoc 1988;83:596–610.
[40] Thompson BG, Brown Jr RD, Amin-Hanjani S, Broderick JP, Cockroft KM, Connolly Jr ES, et al. Guidelines for the management of patients with unruptured intracranial aneurysms: a guideline for healthcare professionals from the American Heart Association/American Stroke Association. Stroke 2015;46:2368–400.
[41] Sanchez S, Hickerson M, Patel RR, Ghazaleh D, Tarchand R, Paranjape GS, et al. Morphological characteristics of ruptured brain aneurysms: a systematic literature review and meta-analysis. Stroke: Vasc Interventional Neurol 2023;3:e000707.